Effects of Parameterized Boundary Layer Structure on Hurricane Rapid Intensification in Shear

JUN A. ZHANG

NOAA/Atlantic Oceanographic and Meteorological Laboratory/Hurricane Research Division,
and Cooperative Institute for Marine and Atmospheric Studies, University
of Miami, Miami, Florida

ROBERT F. ROGERS

NOAA/Atlantic Oceanographic and Meteorological Laboratory/Hurricane
Research Division, Miami, Florida

(Manuscript received 9 January 2018, in final form 28 September 2018)

ABSTRACT

This study investigates the role of the parameterized boundary layer structure in hurricane intensity change using two retrospective HWRF forecasts of Hurricane Earl (2010) in which the vertical eddy diffusivity K_m was modified during physics upgrades. Earl undergoes rapid intensification (RI) in the low-K_m forecast as observed in nature, while it weakens briefly before resuming a slow intensification at the RI onset in the high-K_m forecast. Angular momentum budget analysis suggests that K_m modulates the convergence of angular momentum in the boundary layer, which is a key component of the hurricane spinup dynamics. Reducing K_m in the boundary layer causes enhancement of both the inflow and convergence, which in turn leads to stronger and more symmetric deep convection in the low-K_m forecast than in the high-K_m forecast. The deeper and stronger hurricane vortex with lower static stability in the low-K_m forecast is more resilient to shear than that in the high-K_m forecast. With a smaller vortex tilt in the low-K_m forecast, downdrafts associated with the vortex tilt are reduced, bringing less low-entropy air from the midlevels to the boundary layer, resulting in a less stable boundary layer. Future physics upgrades in operational hurricane models should consider this chain of multiscale interactions to assess their impact on model RI forecasts.

1. Introduction

The vertical shear of the environmental wind is recognized to be a key parameter regulating the intensity and intensity change of tropical cyclones (TCs) (e.g., DeMaria 1996; Kaplan and DeMaria 2003; Zhang and Tao 2013; Kaplan et al. 2015). The TC vortex and environmental shear interaction has been extensively studied by both numerical simulations and observations. Several key mechanisms have been identified to be responsible for shear-induced variation of TC intensity: balanced-dynamical adjustment of a TC vortex to shear-induced vortex tilt (e.g., Jones 1995, 2000; Reasor and Montgomery 2001, 2015), growth of convective asymmetry in the TC eyewall region (e.g., Frank and Ritchie 2001; Ritchie and Frank 2007; Guimond et al. 2010; Jiang 2012), asymmetric organization of TC eye–eyewall mesovortices (e.g., Schubert et al. 1999; Braun et al. 2006; Braun and Wu 2007; Reasor et al. 2009), ventilation of the TC warm core (e.g., Simpson and Riehl 1958; Tang and Emanuel 2012), and modulation of the boundary layer entropy by asymmetric convective downdrafts tied to vortex tilt (e.g., Shelton and Molinari 2009; Riemer et al. 2010; Zhang et al. 2013; Zawislak et al. 2016; Nguyen et al. 2017; Wadler et al. 2018).

The abovementioned mechanisms typically help reveal how and why TCs weaken in a sheared environment. Nonetheless, TCs that are experiencing relatively

---

Denotes content that is immediately available upon publication as open access.

Corresponding author: Jun Zhang, jun.zhang@noaa.gov

DOI: 10.1175/MWR-D-18-0010.1

moderate shear (typically defined as a difference of ~5–10 m s^{-1} between 850 and 200 hPa) occasionally undergo rapid intensification (RI; e.g., Molinari and Vollaro 2010; Nguyen and Molinari 2012). Reasor and Eastin (2012) showed that Hurricane Guillermo (1997) underwent RI in a shear of ~8 m s^{-1}, emphasizing Guillermo's resilience to explain how it underwent RI in this shear environment. Hurricane Earl (2010) was another TC that underwent RI under moderate shear (~6 m s^{-1}). The evolution of the convection of Earl has been studied by Rogers et al. (2015) using Doppler radar data. They found that RI onset occurred once a cluster of deep convection, termed "convective bursts" in that study, became located in the upshear-left quadrant of Earl. A similar result for Earl was found using ground-based lightning data (Stevenson et al. 2014) and passive microwave satellite data (Susca-Lopata et al. 2015). During this same time period of convective bursts, the vortex of Earl became aligned between 2- and 8-km altitude, suggesting that alignment was a precursor to RI onset. Chen and Gopalakrishnan (2015), in a modeling study of Earl, also focused on the azimuthal distribution of convective bursts during RI. They emphasized the role of asymmetric convective bursts in the warm-core development and the linkage to the central pressure drop of Earl. Recently, Zawislak et al. (2016) and Rogers et al. (2016) also highlighted the importance of the azimuthal location of deep convection on the intensification of Hurricane Edouard (2014) using extensive aircraft and satellite observations, finding again that a key feature distinguishing a period of intensification in Edouard was the presence of deep convection on the upshear-left side.

It is also well known that the TC boundary layer plays an important role in changes of TC intensity and structure (e.g., Emanuel 1995; Braun and Tao 2000; Nolan et al. 2009; Sitkowski and Barnes 2009; Smith and Thomsen 2010; Kepert 2012; Bryan 2012; Cione et al. 2013; Zhu et al. 2014; Kilroy et al. 2016; Bu et al. 2017; Williams 2017; Zhang and Pu 2017). Convergence in the boundary layer governs the radial location of updrafts and deep convection, which has been identified as an important mechanism for TC intensification (e.g., Miyamoto and Takemi 2015; Rogers et al. 2015, 2016; Zhang et al. 2017) from theoretical studies that consider the efficiency of diabatic heating in producing temperature changes (and, from balance considerations, TC intensification) (Shapiro and Willoughby 1982; Schubert and Hack 1982; Nolan et al. 2007). When deep convection is located in the region of high inertial stability inside the radius of the maximum wind speed (RMW), the TC typically intensifies at a faster rate than when deep convection is located outside the RMW (e.g., Vigh and Schubert 2009; Pendergrass and Willoughby 2009; Rogers et al. 2013).

Smith and Montgomery (2016) noted limitations in the above theoretical argument and proposed an alternate explanation for why the radial location of deep convection relative to the RMW is crucial for TC intensification. They argued that angular momentum surfaces can be advected inward toward the TC center in the boundary layer if deep convection is located inward from the RMW. Following a similar line of reasoning, angular-momentum convergence in the frictional boundary layer and its role in TC intensification was the focus of several studies (e.g., Smith et al. 2009; Montgomery et al. 2014; Sanger et al. 2014; Montgomery and Smith 2014; Smith et al. 2017) that argued that agradient forcing in the boundary layer helps spin up a TC vortex when the inflowing air radially advects absolute angular momentum at a rate that exceeds that removed by the frictional torque, which is referred to as the boundary layer spinup mechanism.

Although substantial efforts have been made to improve operational TC models in order to advance their skills for track and intensity forecasts (Gopalakrishnan et al. 2013; Tallapragada et al. 2014), it remains a challenging task to accurately forecast TCs undergoing RI (Kaplan et al. 2015), likely because of the continued poor representation of the abovementioned physical processes in the models. As part of the Hurricane Forecast Improvement Project (HFIP; Gall et al. 2013), a recent upgrade of the boundary layer physics in the operational Hurricane Weather Research and Forecasting (HWRF) Model was completed. One of these upgrades was the vertical eddy diffusivity K_m in the planetary boundary layer (PBL) scheme, which was reduced to be more consistent with airborne in situ observations given by Zhang et al. (2011) and Zhang and Drennan (2012). Zhang et al. (2017) studied the impact of this improvement on RI prediction, showing substantially improved RI detection. They also showed that TCs in HWRF forecasts with this reduced K_m tend to retain stronger inflow in a shallower boundary layer at RI onset. Deeper and stronger updrafts (i.e., deep convection) are shown to be farther inward from the RMW at the RI onset, which is consistent with stronger boundary layer convergence in the HWRF forecasts with smaller K_m than with larger K_m.

Note that Zhang et al. (2017) only focused on model diagnostics of the axisymmetric TC structure using a composite approach due to computational limitations. As a follow-up to Zhang et al. (2017), the present study evaluates the role of the parameterized boundary layer structure in modulating the asymmetric TC structure associated with RI. A case study approach is used here instead, to analyze two HWRF retrospective forecasts of Hurricane Earl (2010), a TC that underwent RI in moderate shear. Building upon previous studies on TC and shear interactions, the objective of this case study is to further explore why changes in the boundary layer structure led to a different evolution of deep convection and vortex tilt and evaluate their feedback to the boundary layer and in turn TC intensification. Specifically, we intend to address the following questions:

1) How does K_m affect the radial advection of angular momentum in the boundary layer and its relative role in vortex spinup?
2) How does K_m-induced change in the boundary layer structure affect the distribution of deep convection and RI?
3) How does K_m influence the evolution of vortex tilt and its feedback to boundary layer thermodynamics?
4) How does K_m influence the distribution of surface enthalpy fluxes and the boundary layer recovery process?

2. HWRF forecasts of Hurricane Earl (2010)

As mentioned earlier, the HWRF retrospective forecasts are used to study the impact of parameterized boundary layer structure on hurricane intensity change. The description of the HWRF Model and retrospective forecasts parallels that of Zhang et al. (2015, 2017) in the next two paragraphs with minor modification. The HWRF system was initially developed at the Environmental Modeling Center (EMC) of the National Weather Service (NWS). During the past eight years, joint development of HWRF was also accomplished at the Hurricane Research Division (HRD) in collaboration with EMC as part of HFIP. Below we only briefly describe the PBL scheme of the version (V3.7) of HWRF used in this study, while descriptions of other components of the model physics as well as the initial and boundary conditions can be found in Tallapragada et al. (2014) and Zhang et al. (2015).

The PBL scheme used here is essentially a modified version of the Medium-Range Forecast (MRF) scheme (Troen and Mahrt1986) that has been used in the Global Forecast System (GFS) for more than a decade. In this scheme, turbulent fluxes in the boundary layer are parameterized by K_m following the standard downgradient assumption (Hong and Pan 1996; Gopalakrishnan et al. 2013; Zhang et al. 2015), in which K_m has the form of

$$K_m = \kappa(u^*/S)z[\alpha(1-z/h)^2], \tag{1}$$

where $\kappa = 0.4$ is the Von Kármán constant; α is a parameter controlling the magnitude and shape of K_m, which was added to the PBL scheme of HWRF in 2012; u^* is the frictional velocity; S is the surface layer stability function; z is the height; and h is the boundary layer height that is defined based on a critical Richardson number. Note that K_m calculated using $\alpha = 0.5$ better matches with observational estimates given by Zhang et al. (2011) and Zhang and Drennan (2012) than that calculated using $\alpha = 1$ as in the earlier version of the HWRF Model [see Fig. 1 of Zhang et al. (2017)], notwithstanding the limitations of this α method as detailed by Zhang et al. (2012, 2015, 2017). We note also that Braun and Tao (2000) are the first who have pointed out that the boundary layer is too diffusive in hurricane simulations with the MRF-type PBL scheme. Other numerical studies (e.g., Smith and Thomsen 2010; Kepert 2012) also pointed out the limitation of using the MRF-type PBL scheme to simulate the TC boundary layer structure.

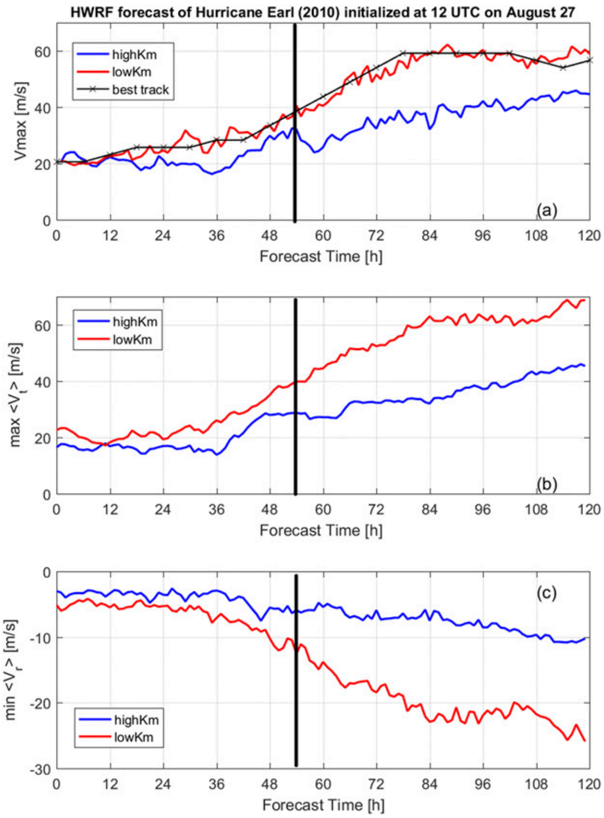

FIG. 1. Time series of (a) the storm intensity in terms of the maximum surface wind speed, (b) maximum azimuthally averaged tangential wind speed V_t, and (c) minimum azimuthally averaged radial wind speed, from two HWRF forecasts of Hurricane Earl (2010) initialized at 1200 UTC 27 Aug 2010 with high-K_m and low-K_m boundary layer physics. The black line indicates the intensity divergence point at $t = 54$ h.

As detailed by Zhang et al. (2015), two sets of HWRF retrospective forecasts of over 100 cases were conducted by EMC with $\alpha = 0.5$ (referred to as low-K_m hereafter) and $\alpha = 1$ (referred to as high-K_m hereafter),

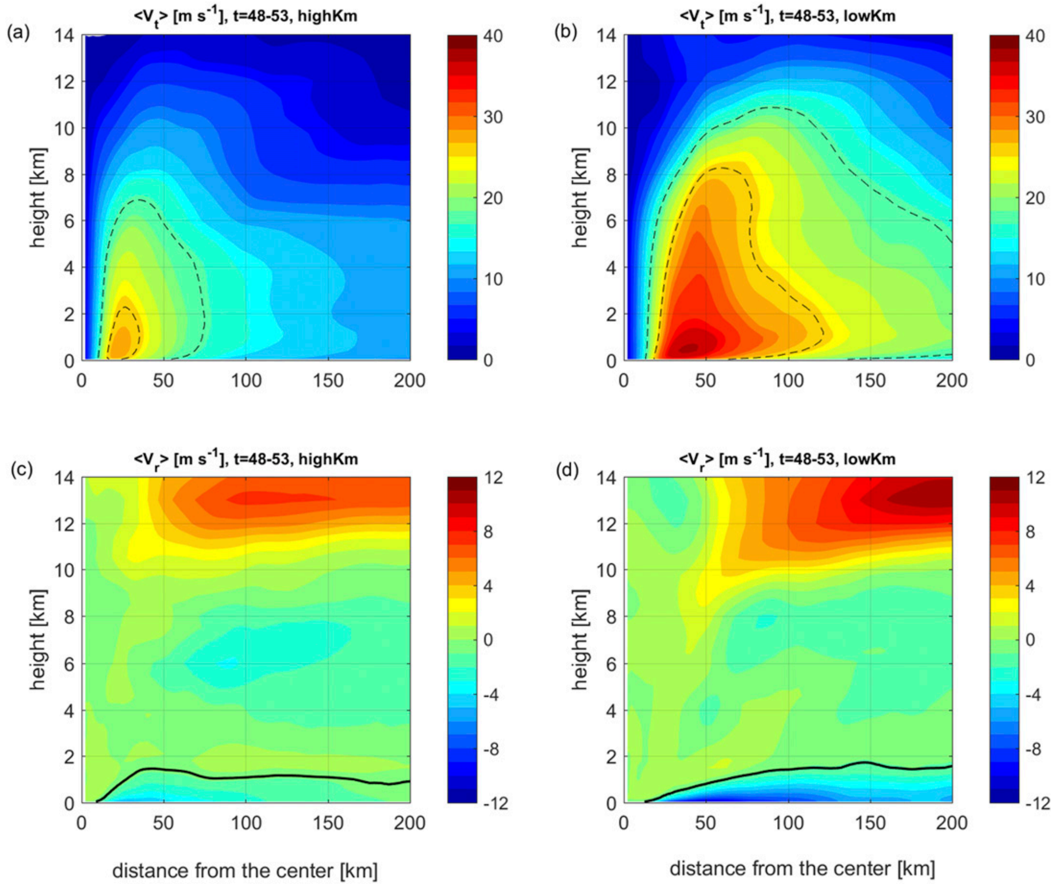

FIG. 2. The radius–height plot of the (a),(b) azimuthally averaged tangential wind speed and (c),(d) radial wind speed during the period of 48–53 h in (left) high-K_m forecast and (right) low-K_m forecast. The black dashed lines in (a) and (b) denote contours of 64 and 34 kt, respectively. The black line in (c) and (d) denotes the inflow layer depth defined as the height of 10% peak inflow.

respectively. These forecasts were run in a cycling mode,[1] using the same initial conditions at the first forecast of Earl boundary conditions, and the same physics, except for this α parameter in the PBL scheme. In this study, we focus on analyzing two HWRF forecasts of Hurricane Earl (2010) that are initialized at 1200 UTC 27 August 2010: one from high-K_m and the other from low-K_m forecasts. The storm intensity from these two forecasts, as measured by the peak 10-m wind speed ($V_{\max}$), is shown in Fig. 1a. The storm intensity is similar between the two forecasts in the first 36 h, remaining nearly steady state. After that time, the storm in both forecasts slowly intensifies. However, the intensity forecast shows a bifurcation (i.e., divergence in intensity forecast) at ~54 h, when the storm in the high-K_m forecast weakens briefly before resuming a slow intensification, while the storm keeps intensifying in the low-K_m forecast until reaching its maximum intensity at 84 h. The intensity forecast from low-K_m closely follows the best-track intensity. The evolution of the maximum azimuthally averaged tangential velocity (max $<V_t>$) and minimum radial velocity (min $<V_r>$; i.e., inflow strength) in the eyewall is shown in Figs. 1b and 1c, respectively, indicating that both the primary and secondary circulations of Earl develop much faster in the low-K_m forecast than in the high-K_m forecast, consistent with the intensity forecasts. Prior to the intensity divergence point, the axisymmetric vortex, as measured by the azimuthal mean tangential velocity, is weaker and shallower in the high-K_m forecast than in the low-K_m forecast (Figs. 2a and 2b). Furthermore, the inflow is much stronger in the low-K_m forecast than that in the high-K_m forecast in the boundary layer (Figs. 2c and 2d).

---

[1] A cycling mode means the HWRF Model was run every 6 h from the initial time of the forecast. At each cycle, vortex initialization and data assimilation were turned on, which makes the initial intensity of the storm the same but the vortex structure could be different.

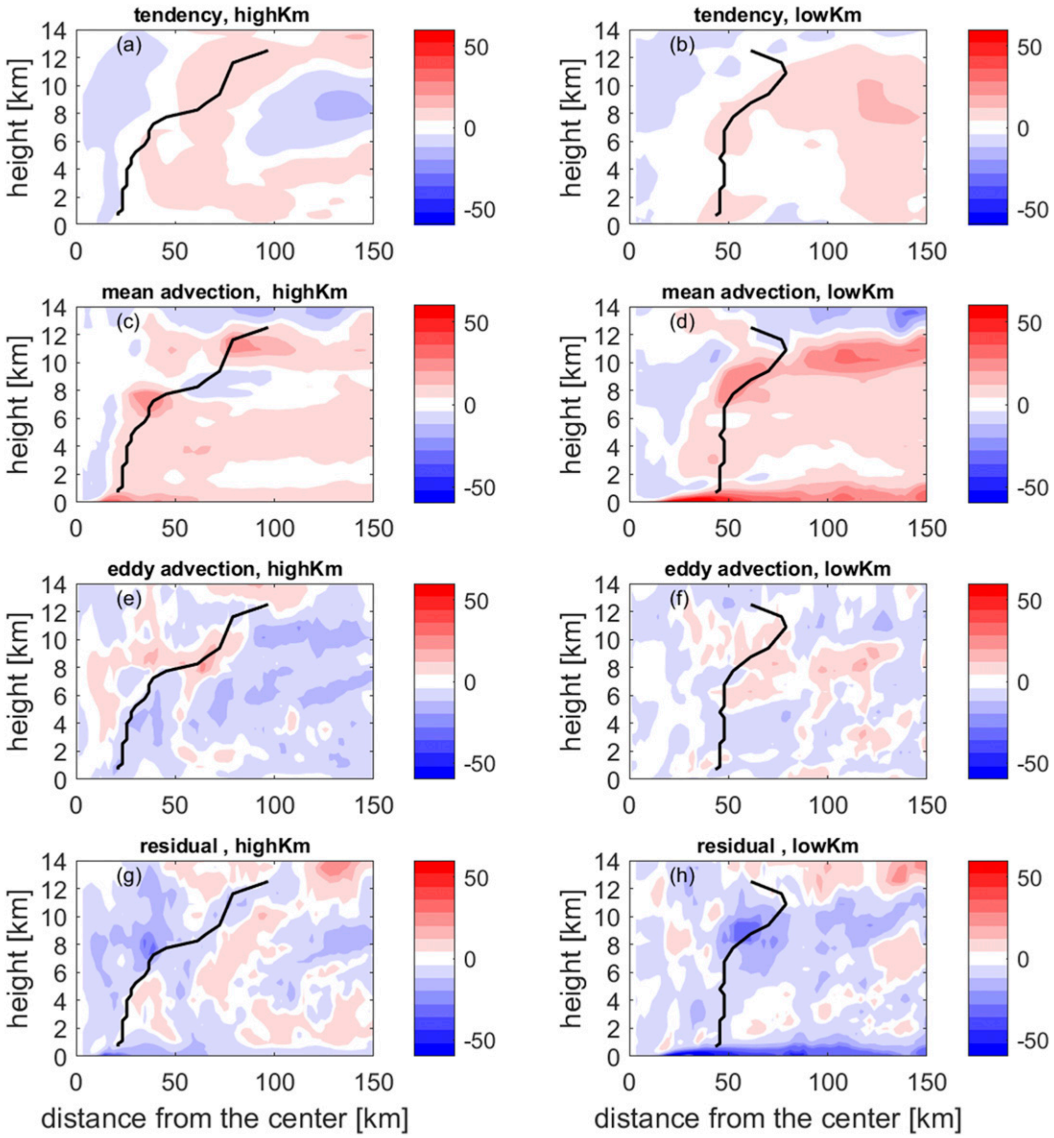

FIG. 3. The radius–height plot of the terms in the absolute angular momentum (M) budget for the (left) high-K_m and (right) low-K_m forecast during a period (48–50 h). The budget terms consist of (a),(b) the local rate of change of $<M>$; (c),(d) the total mean advection of $<M>$; (e),(f) the sum of the eddy transport of $<M'>$; and (g),(h) the friction term F_r. The black line denotes the radius of maximum azimuthally averaged tangential wind speed. Note that the residual term equals the tendency term minus the sum of the mean and eddy transport terms. All terms are expressed in units of $10^6\,\mathrm{m^2\,s^{-1}\,h^{-1}}$.

3. Angular momentum budget

We first look into mechanisms that may dynamically contribute to the difference in the intensity change between the high-K_m and low-K_m forecasts of Hurricane Earl. Budget analyses of the absolute angular momentum ($M = rV_t + 2fr^2$, where r is radial distance and f is the Coriolis frequency) are conducted. Note that the method and description of the angular momentum budget parallels that given by Zhang and Marks (2015) in the following three paragraphs.

The budget equation of the azimuthally averaged M tendency has the form of

$$\begin{aligned}\frac{\partial\langle M\rangle}{\partial t} &= -\langle V_r\rangle\frac{\partial\langle M\rangle}{\partial r} - \langle w\rangle\frac{\partial\langle M\rangle}{\partial z}\\ &\quad - \left\langle V_r'\frac{\partial M'}{\partial r}\right\rangle - \left\langle w'\frac{\partial M'}{\partial z}\right\rangle + F_r,\end{aligned} \tag{2}$$

where w is the vertical velocity. The bracket represents an azimuthal average at a given height, and the prime represents a departure from the azimuthal mean (or "eddy" term). Here, the three velocity components are storm relative. Terms on the right-hand side of Eq. (2) are the mean radial advection of $<M>$, the mean vertical advection of $<M>$, the radial eddy transport of $<M>$, the vertical eddy transport of $<M>$, and the residual term (F_r), respectively. Of note, the residual term, F_r, includes both the vertical and horizontal diffusion associated with subgrid turbulent processes. Although diffusive terms are not explicitly output, budget analyses based on a research version of HWRF with the same setup in the operational version as used in this study confirmed that the terms are balanced (Smith et al. 2017; Leighton et al. 2018). Note also that Eq. (2) follows the absolute angular momentum budget given by Smith et al. (2009) except the eddy transport terms are included here as well.

We first look into the role of mean and eddy transport terms in the total $<M>$ budget that is affected by the change in K_m. For simple comparison purposes, the tendency of $<M>$, the total mean and eddy transport of $<M>$, and the F_r term are shown in Fig. 3 from the high-K_m (left panels) and low-K_m (right panels) forecasts. Here, all the budget terms shown in Fig. 3 are averaged over the period of 48–50 h. The $<M>$ tendency is generally larger in the low-K_m forecast than in the high-K_m forecast (Figs. 3a and 3b) consistent with the intensity forecasts. In addition, the $<M>$ tendency in the low-K_m forecast is mostly positive, while that in the high-K_m forecast has a layer of negative values over positive values. The low-K_m tends to spin up the flow everywhere outside of the eye, and particularly at low levels at the RMW, while high-K_m only spins up low to midlevels outside of the RMW.

In both high-K_m and low-K_m forecasts, the total mean advection term contributes more to the total tendency of $<M>$ than the eddy advection term in the boundary layer. However, the mean advection term is substantially larger in the low-K_m forecast than in the high-K_m forecast (Figs. 3c,d), especially in the boundary layer, which is mainly due to the stronger low-level inflow induced by the smaller K_m in the low-K_m forecast. The result of the eddy contribution to the total $<M>$ in the two forecasts is consistent in producing a positive tendency along the eyewall at the mid- to upper levels while producing a negative tendency at lower levels in the eyewall region. The eddy term in the high-K_m (Fig. 3e) forecast is more positive inside the RMW at 3–10-km altitude, than the low-K_m (Fig. 3f) forecast, while it is more negative below 3-km altitude inside the RMW.

Note that the spinup of the vortex in the boundary layer due to the positive mean advection of $<M>$ is mainly from the radial advection of $<M>$. The radial advection of $<M>$ exceeds the boundary layer diffusion caused by subgrid processes in the low-K_m forecast when the storm intensifies, which is consistent with the spinup theory of Smith et al. (2009) that emphasized the importance of the boundary layer spinup mechanism. The stronger boundary layer inflow induced by smaller K_m makes the radial advection of high $<M>$ much larger and the spinup of the storm much faster in the low-K_m forecast than in the high-K_m forecast.

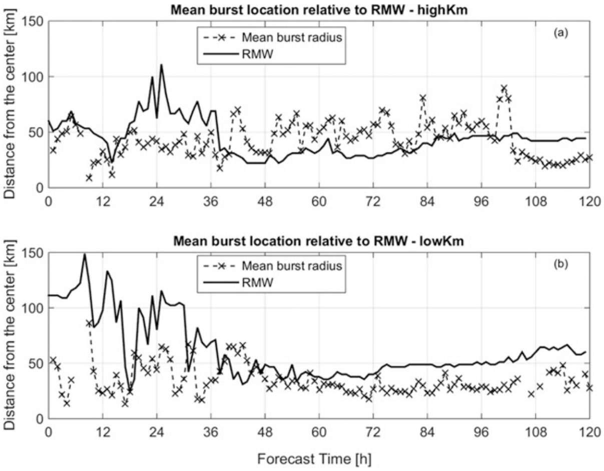

FIG. 4. Time evolution of the mean radius of convective bursts and the radius of maximum wind speed (RMW) at 2 km for the (a) high-K_m and (b) low-K_m forecasts of Hurricane Earl (2010).

4. Distribution of deep convection

Next, we evaluate the impact of K_m on the distribution of deep convection (hereafter referred to as convective bursts).[2] The evolution of the mean radial location of bursts within 200 km from the storm center and the radius of azimuthally averaged maximum wind speed at 2-km altitude (RMW) is shown in Fig. 4. It is evident that the mean radial location of the bursts is mostly within the RMW in the low-K_m forecast, while it is outside the RMW in the high-K_m forecast, especially after the intensity divergence point ($t = 54$) of the intensity forecast (Fig. 1a). The count of convective bursts 6 h before the intensity divergence point ($t = 54$) as a function of radius to the storm center normalized by the RMW is shown in Figs. 5a and 5b, respectively, for the high-K_m and low-K_m forecasts. Here, we break the bars into three groups showing the

---

[2] We define a convective burst as locations where the maximum vertical velocity in the vertical column of each model grid point is $>3\,\mathrm{m\,s^{-1}}$, following previous modeling studies (Chen and Zhang 2013; Chen and Gopalakrishnan 2015).

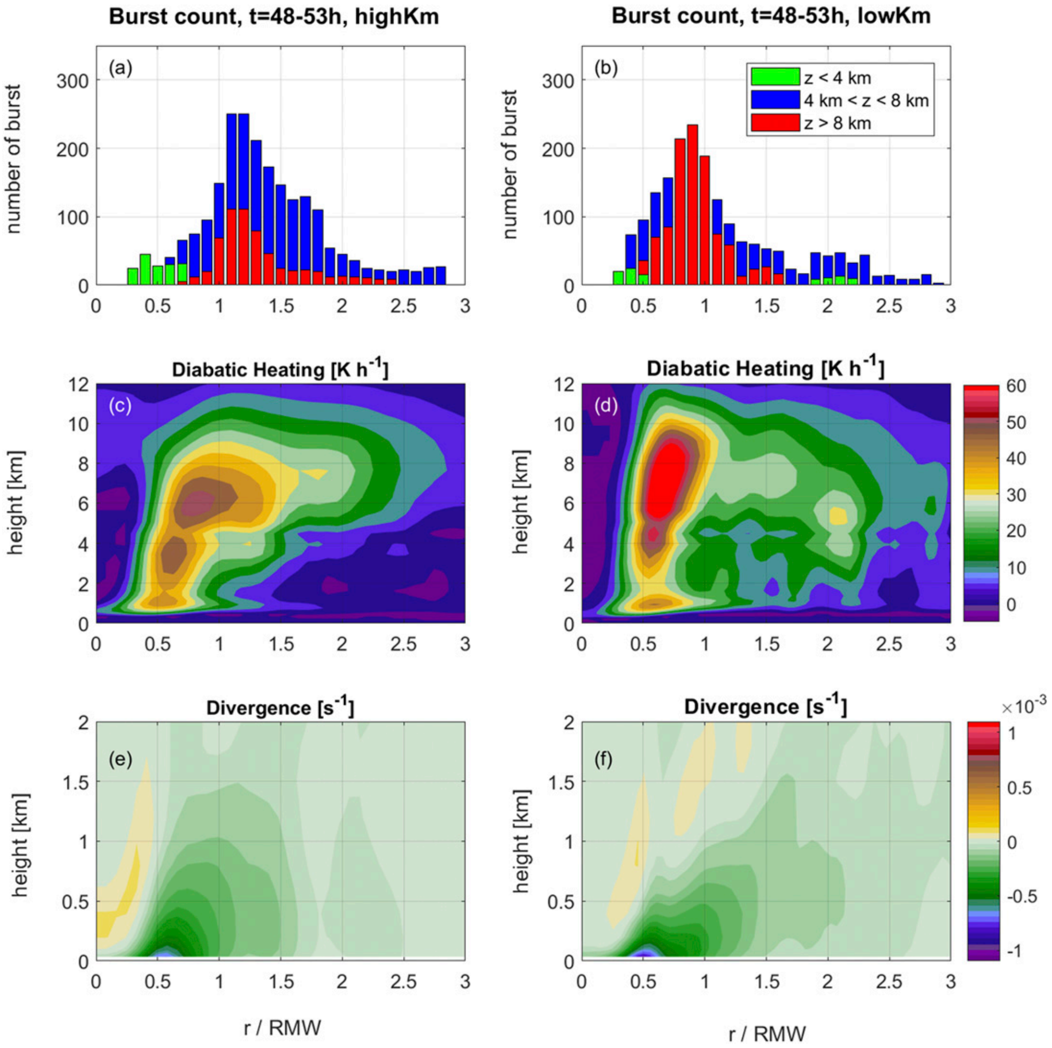

FIG. 5. The plot of the number of convective bursts as a function of radius normalized by RMW at 2 km for (a) high-K_m and (b) low-K_m forecasts during the period between 48 and 53 h of forecast time; the azimuthally averaged diabatic heating averaged during this period as a function of radius normalized by RMW at 2 km for (c) high-K_m and (d) low-K_m forecasts, and the azimuthally averaged divergence averaged during this period as a function of radius normalized by RMW at 2 km for (e) high-K_m and (f) low-K_m forecasts. The burst counts are grouped into three groups showing the burst distribution below 4 km (green), between 4 and 8 km (blue) and above 8 km (red).

number of bursts below 4 km, between 4 and 8 km, and above 8 km. The majority of the bursts are located at and inside the RMW (0.5–1 RMW) for the low-K_m forecast, but most of the bursts are located outside the RMW (1–2 RMW) for the high-K_m forecast, especially for the bursts at higher altitudes. This result in the low-K_m forecast is consistent with burst observations of Hurricane Earl documented by Rogers et al. (2015) and supports the theoretical argument of Smith and Montgomery (2016).

The azimuthally averaged diabatic heating rate in the low-K_m forecast is found to be much larger, and more radially concentrated, than that in the high-K_m forecast, especially inside the RMW (Figs. 5c and 5d). Interestingly, in both the low-K_m and high-K_m forecasts, the largest azimuthally averaged diabatic heating is located mainly inside the low-level RMW, while the mean burst location is different. The radial location of the maximum diabatic heating may be tied to that of the maximum boundary layer convergence. It is evident from Figs. 5e and 5f that the peak boundary layer convergence is located inside the low-level RMW in both forecasts, which is shifted slightly inward in the low-K_m forecast. The magnitude of the peak azimuthally averaged boundary layer convergence is much larger in the low-K_m forecast than in the high-K_m forecast

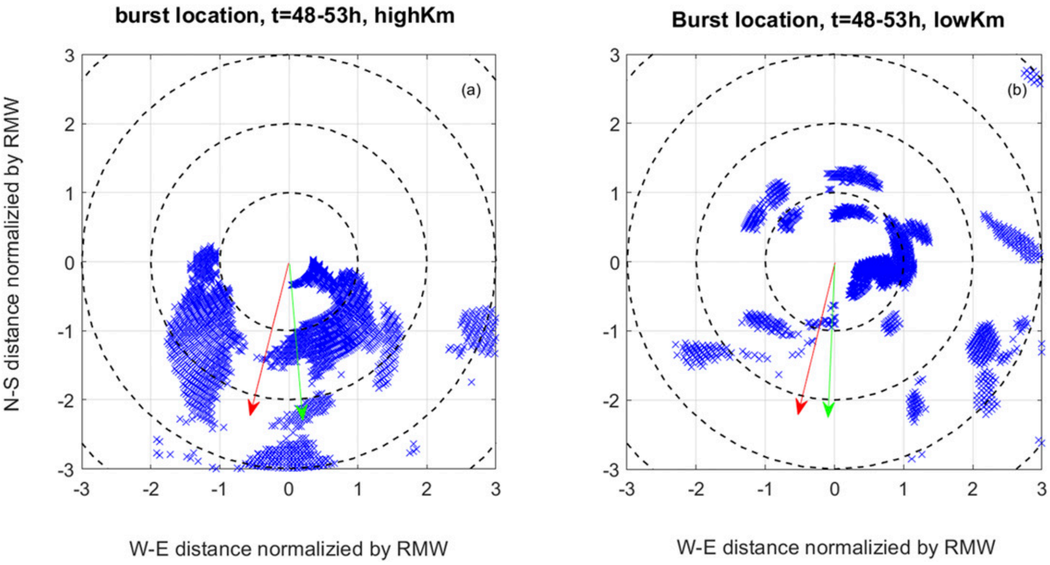

FIG. 6. Horizontal view of burst locations during the period between 48 and 53 h of forecast time for (a) high-K_m and (b) low-K_m forecasts. The red arrow indicates the shear direction. The green arrow indicates the tilt direction. Note that magnitude of the tilt is ~0.7 RMW for high-K_m and is ~0.4 RMW for low-K_m forecasts.

(Figs. 5e and 5f), which correlates well with the peak diabatic heating.

We note that diabatic heating depends on the total mass flux in the eyewall, and convective bursts contribute only a fraction of the total mass flux. Braun (2002) showed that about half of the upward mass flux in his case was associated with updrafts less than 3 m s^{-1} (see their Fig. 11), while Rogers (2010) found that the bulk of the upward mass flux in Hurricane Dennis (2005) was also accomplished by weak to moderate strength drafts. Thus, the difference in the magnitude of the diabatic heating inside the low-level RMW between the low-K_m and high-K_m forecast may be due to differences in the strength of the updrafts including the weaker updrafts that are not classified as bursts. The weaker boundary layer convergence and inflow lead to weaker updrafts exiting the boundary layer in the high-K_m forecast. In addition, diabatic heating–induced secondary circulation above the boundary layer is smaller in the high-K_m forecast according to the conventional hurricane spinup mechanism (Ooyama 1969; Smith et al. 2009) because both the magnitude and the radial and vertical gradients of the diabatic heating rate are smaller in the high-K_m forecast than in the low-K_m forecast.

The radial distribution of the burst counts may also be impacted by the altitude of the bursts/slope of the eyewall. It is evident from Figs. 5c and 5d that the symmetric diabatic heating rate is substantially higher outside the RMW above 8-km altitude in the high-K_m forecast compared with the low-K_m forecast. These differences in symmetric diabatic heating are generally consistent with the burst distributions as a function of altitude as seen in Figs. 5a and 5b. The fact that the bursts tend to stay outside the low-level RMW may be due to the more outward-sloped eyewall relative to the low-level RMW in the high-K_m forecast compared with the low-K_m forecast.

Furthermore, the difference in the magnitude of the symmetric diabatic heating rate above 8 km may also be tied to the difference in the azimuthal distribution of the bursts in the two forecasts. The horizontal view of the convective bursts indicates that the azimuthal distribution of the bursts in the eyewall region (~r/RMW = 1) is more symmetric in the low-K_m forecast than in the high-K_m forecast (Fig. 6), resulting in a greater projection of diabatic heating onto the azimuthal mean for low-K_m from the convective bursts.

In the low-K_m forecast of Hurricane Earl (2010), the majority of the inner-core bursts are mostly located in the downshear (tilt) direction to left of shear, while the bursts are mainly located in the downshear (tilt) direction in the high-K_m forecast. Here, we define the vortex tilt as the displacement of the storm center[3] from 1 to 8 km. It is evident from Fig. 6 that there are many more bursts located on the upshear side of the storm in the low-K_m forecast than in the high-K_m forecast. The observational study of Earl by Stevenson et al. (2014) noted the presence of lightning in the upshear region starting just before

---

[3] Here, the storm center is defined as the centroid of sea level pressure (e.g., Braun 2002; Wang 2007; Nguyen et al. 2014). Other methods such as using the minimum sea level pressure and centroid of vorticity to compute the storm center give similar tilt magnitude in this case study.

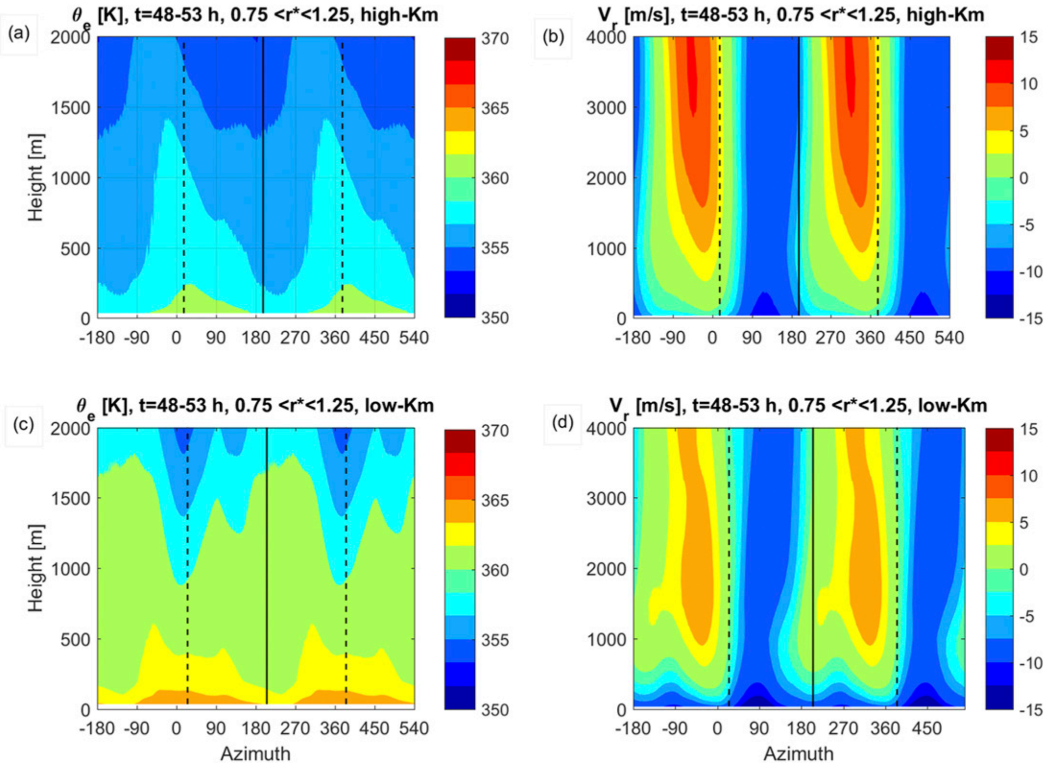

FIG. 7. Azimuth–height plot of (left) equivalent potential temperature θ_e and (right) radial velocity V_r averaged in a period of 48–53 h at the radial band of 0.75–1.25r^* from (a),(b) the high-K_m forecast and (c),(d) the low-K_m forecast. The dotted lines represent the upshear direction. The azimuth 0° = north of the TC center, 90° = east, 180° = south, and 270° = west.

RI, while the observational study of Hurricane Edouard (2014; Rogers et al. 2016) also noted deep convection on the upshear side before and during rapid intensification. The more symmetric distribution of deep convection in the low-K_m forecast is expected to favor vortex alignment (shown later in section 5). In a similar manner as in Hurricane Earl, Munsell et al. (2017) showed that vortex alignment generally occurred just prior to RI in Hurricane Edouard in their ensemble simulations.

The azimuthal distribution of the bursts is found to be correlated to that of the boundary layer entropy (i.e., equivalent potential temperature θ_e) and inflow. Figure 7 shows that both the low-level (<1 km) θ_e and inflow are more symmetric in the low-K_m forecast than in the high-K_m forecast in the eyewall region ($0.75 < r^* < 1.25$). Note that the degree of asymmetry is quantified based on the same asymmetric metric as that used by Reasor et al. (2013) (i.e., the azimuthal standard deviation of a field within the prescribed radial band). The azimuthal standard deviation of θ_e averaged below 1-km altitude is 0.67 K in the high-K_m forecast versus 0.53 K in the low-K_m forecast. The azimuthal standard deviation of the inflow averaged below 1-km altitude is 4.4 m s^{-1} in the high-K_m forecast versus 3.3 m s^{-1} in the low-K_m forecast. As the boundary layer moisture is the main energy source to maintain the deep convection, a more symmetric distribution of low-level θ_e favors more evenly distributed deep convection in the low-K_m forecast. The stronger and more symmetric boundary layer inflow in the low-K_m forecast can bring higher entropy air into the eyewall before turning to upward motion inside the RMW, favoring the development of convection in the low-K_m forecast. We will show later that both convective downdrafts (in section 5) and surface fluxes (in section 6) modulate the azimuthal distribution of low-level θ_e in response to the change in K_m.

5. Vortex tilt and feedback to boundary layer thermal structure

Previous studies have suggested that vortex tilt is an important aspect of sheared storms (e.g., Jones 1995; Reasor et al. 2000). Figure 8a shows the evolution of the vortex tilt magnitude and direction from the two Earl forecasts. The magnitude of the tilt in the high-K_m and low-K_m forecasts is comparable before 47 h with tilt magnitude ranging from 40 to 80 km. After this time, the tilt relaxes to ~15 km in the low-K_m forecast

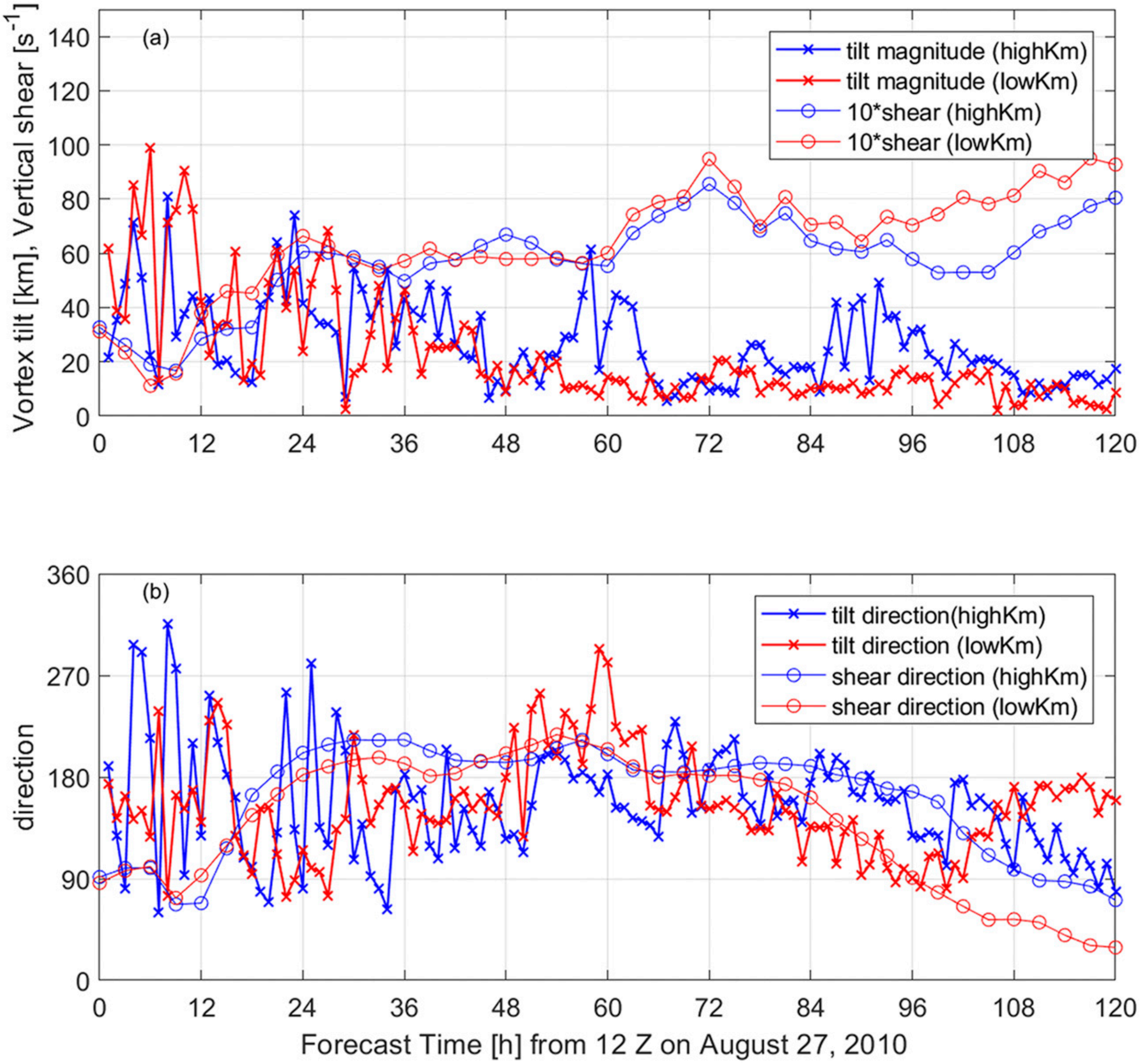

FIG. 8. Plot of vortex tilt (a) magnitude and (b) direction as a function of forecast time for high-K_m and low-K_m forecasts of Hurricane Earl (2010). Here the vortex tilt is defined as the storm center displacement from 1 to 8 km, and the storm center is defined as the location of the minimum horizontal wind speed. The shear magnitude and direction are also shown in the lines with circles. The azimuth 0° = north of the TC center, 90° = east, 180° = south, and 270° = west.

and stays nearly constant thereafter. However, the tilt in the high-K_m forecast oscillates from 15 to 60 km with a period of approximately 30 h in a tilt precession process. It is at around the intensity divergence point ($t = 54$ h) of the intensity forecasts for high-K_m and low-K_m that the vortex tilt magnitude becomes different in these two forecasts. The direction of tilt for each forecast mainly stays close to the downshear direction (Fig. 8b).

The difference in the tilt evolution can be attributed to the vortex-scale structural difference between the two forecasts. As mentioned earlier, before the intensity divergence point, the vortex of Earl is stronger and deeper in the low-K_m forecast than in the high-K_m forecast (cf. Fig. 2), which makes it more resilient to the wind shear in the low-K_m forecast according to the hurricane vortex-alignment theory given by Reasor and Montgomery (2001). The oscillation noted in the vortex tilt magnitude in the high-K_m forecast can also be explained by theory. Jones (1995) also showed that the tilt magnitude during precession is larger for smaller and weaker hurricane vortices.

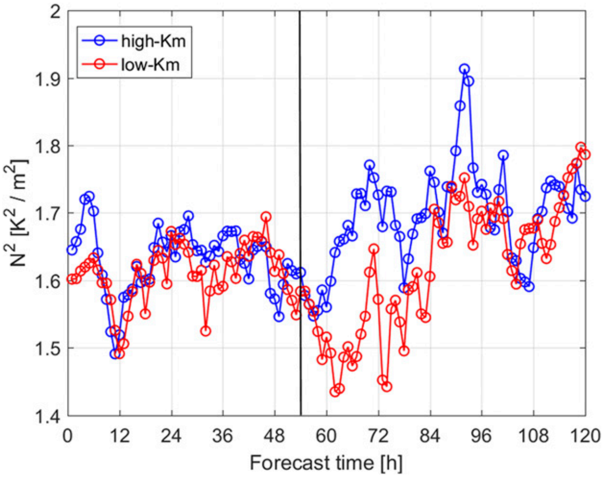

FIG. 9. The plot of the static stability N^2 averaged in the eyewall region ($0.75 < r^* < 1.25$) between 6- and 16-km altitude as a function of forecast time for the high-K_m forecast (blue) and low-K_m forecast (red). The black line indicates the intensity divergence point at $t = 54$ h.

The static stability of a TC vortex is also linked to the vortex tilt evolution according to previous studies on tilt dynamics (Jones 1995; Schecter et al. 2002; Schecter 2015; Reasor and Montgomery 2015). For instance, Jones (1995) pointed out that, from a quasi-geostrophic point of view, vortex tilt decreases with increasing penetration depth of a potential vorticity anomaly, and the penetration depth is inversely correlated with the static stability. Both dry balance (Reasor et al. 2004) and moist balance theory (Schecter 2015; Reasor and Montgomery 2015) for vortex alignment pointed out that the static stability affects the efficiency of the vortex–Rossby wave damping mechanism for vortex tilt reduction. The decrease in the static stability would favor the reduction in tilt magnitude from these abovementioned theoretical studies. Figure 9 shows the static stability (N^2) averaged in the eyewall region ($0.75 < r^* < 1.25$) in the mid- to upper troposphere (i.e., between 6- and 16-km altitude) as a function of forecast time. The atmosphere is much more stable in the high-K_m forecast than in the low-K_m forecast, especially after the intensity divergence point, which makes the vortex more vulnerable to shear than the vortex in the low-K_m forecast, consistent with the vortex alignment theories. It is likely that the reduction of the static stability in the low-K_m forecast is due to the enhancement of moist convection following the argument of Schecter and Montgomery (2007).

As discussed by Riemer et al. (2010, 2013), vortex tilt could lead to downdraft cooling and an associated reduction in θ_e in the boundary layer outside the RMW along the direction of vortex tilt. This boundary layer thermodynamic response is evaluated in the high-K_m and low-K_m forecasts of Hurricane Earl (2010). With larger tilt in the high-K_m forecast than in the low-K_m forecast after the intensity divergence point ($t = 54$ h), air with much lower θ_e is seen in both the azimuthally averaged field (Fig. 10) and the horizontal view (Fig. 11) in the high-K_m forecast. It is evident from Figs. 10a and 10c that the lower values of θ_e penetrate to the boundary layer in the eyewall region from above after the large tilt occurs in the high-K_m forecast after the intensity divergence point ($t = 54$ h) of the intensity forecasts. On the other hand, the difference in the boundary layer θ_e between the two periods (48–53 and 54–59 h) is small in the low-K_m forecast, likely due to the nearly aligned vortex (Figs. 10b and 10d).

Figure 11 further illustrates the substantial difference in low-level θ_e between high-K_m and low-K_m forecasts, in that there is a much larger area of low values of θ_e that are collocated with stronger downdrafts in the high-K_m forecast than in the low-K_m forecast. Riemer et al. (2010, 2013) also found a persistent region of downdrafts associated with an asymmetric convective band outside the eyewall region, and this band is tied to asymmetric boundary layer convergence resulting from the outer vortex tilt (Riemer 2016; Riemer and Laliberte 2015). Note that this type of shear-relative θ_e asymmetry in the Earl forecasts is also seen in the dropsonde composite analysis (Zhang et al. 2013) and individual observational studies of sheared TCs (Zawislak et al. 2016; Nguyen et al. 2017).

6. Air–sea fluxes and boundary layer recovery

In addition to vortex tilt and convective asymmetry mentioned above, surface flux is another factor that influences the distribution of the boundary layer θ_e. The total enthalpy fluxes (i.e., the sum of sensible heat and latent heat fluxes) in the high-K_m forecast (Figs. 12a and 12c) are compared to those in the low-K_m forecast (Figs. 12b and 12d) for the two periods: 6 h before and after the intensity divergence point ($t = 54$ h). Before this point, the enthalpy fluxes are of a higher magnitude and cover a broader area in the low-K_m forecast than in the high-K_m forecast. The enthalpy flux is more symmetric in the low-K_m forecast than in the high-K_m forecast, supporting the more symmetric boundary layer θ_e seen in the low-K_m forecast. This larger and more symmetric flux pattern and θ_e distribution support the more symmetric deep convection (cf. Fig. 6), likely driven by a more symmetric and intense vortex, which is consistent with the numerical simulations of Onderlinde and Nolan (2016).

In the first period ($t = 48$–53 h), the vortex tilt is relatively small (~15 km) for both the low-K_m and high-K_m forecasts. The flush of low-θ_e air from the midlevels to

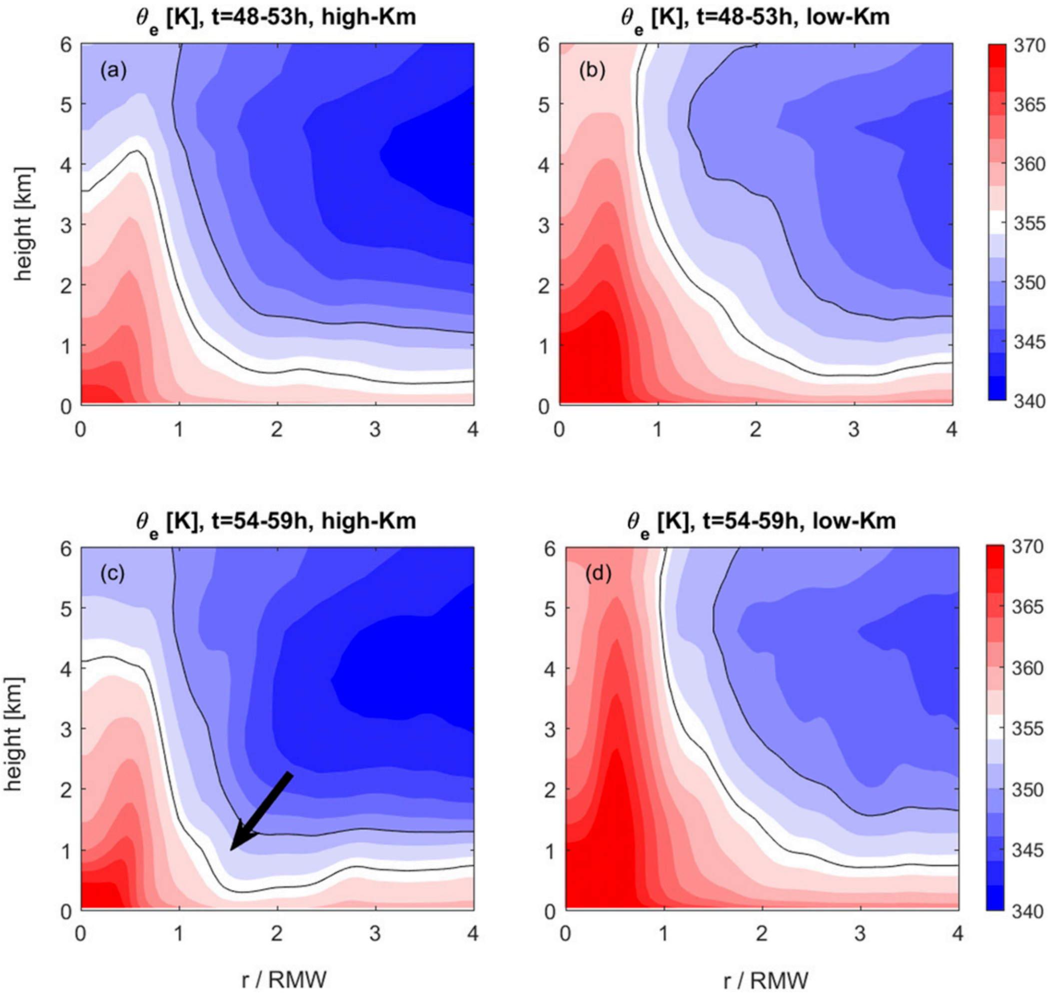

FIG. 10. The radius and height plot of the azimuthally averaged equivalent potential temperature θ_e averaged during two periods: $t = 48$–54 h and $t = 54$–59 h for the (left) high-K_m and (right) low-K_m forecasts of Hurricane Earl (2010). The black lines show the contours of 345 and 355 K. The black arrow indicates the penetration of low θ_e from the midlevel to the boundary layer.

the boundary layer through convective downdrafts associated with the tilt is similar when the tilt magnitude is similar (cf. Fig. 11). Thus, the difference in boundary layer thermal structure between the two forecasts is largely due to the difference in surface fluxes during this period ($t = 48$–53 h), assuming all else remains equal. When surface fluxes become larger, the boundary layer becomes warmer and moister, leading to larger θ_e. As the θ_e increases, the air–sea thermal contrast becomes small, so that the enthalpy flux stops increasing with the increasing wind speed in the low-K_m forecast in the second period ($t = 54$–59 h). In addition, there is less modification of θ_e caused by tilt-induced convective downdrafts in the low-K_m forecast than in the high-K_m forecast during the second period as the tilt is small in the low-K_m forecast during this period.

On the other hand, in the high-K_m forecast, large tilt causes more flush of low-θ_e air from midlevels to the boundary layer and surface layer (cf. Fig. 11); the low-θ_e air then helps increase the air–sea thermal contrast in the high-K_m forecast, so that the peak enthalpy flux becomes as large as that in the low-K_m forecast despite the weaker surface wind speed in the high-K_m forecast. The question is: Are these enthalpy fluxes during the second period of sufficient magnitude such that the downdraft θ_e in the upshear-left quadrant recovers to ambient nondowndraft values by the time the air reaches the downshear-right quadrant?

A simple θ_e budget analysis following Molinari et al. (2013) and Zhang et al. (2013, 2017) suggested that in the eyewall region ($r^* \sim 1$, where $r^* = r$/RMW, and r is the radius), surface enthalpy fluxes are enough to

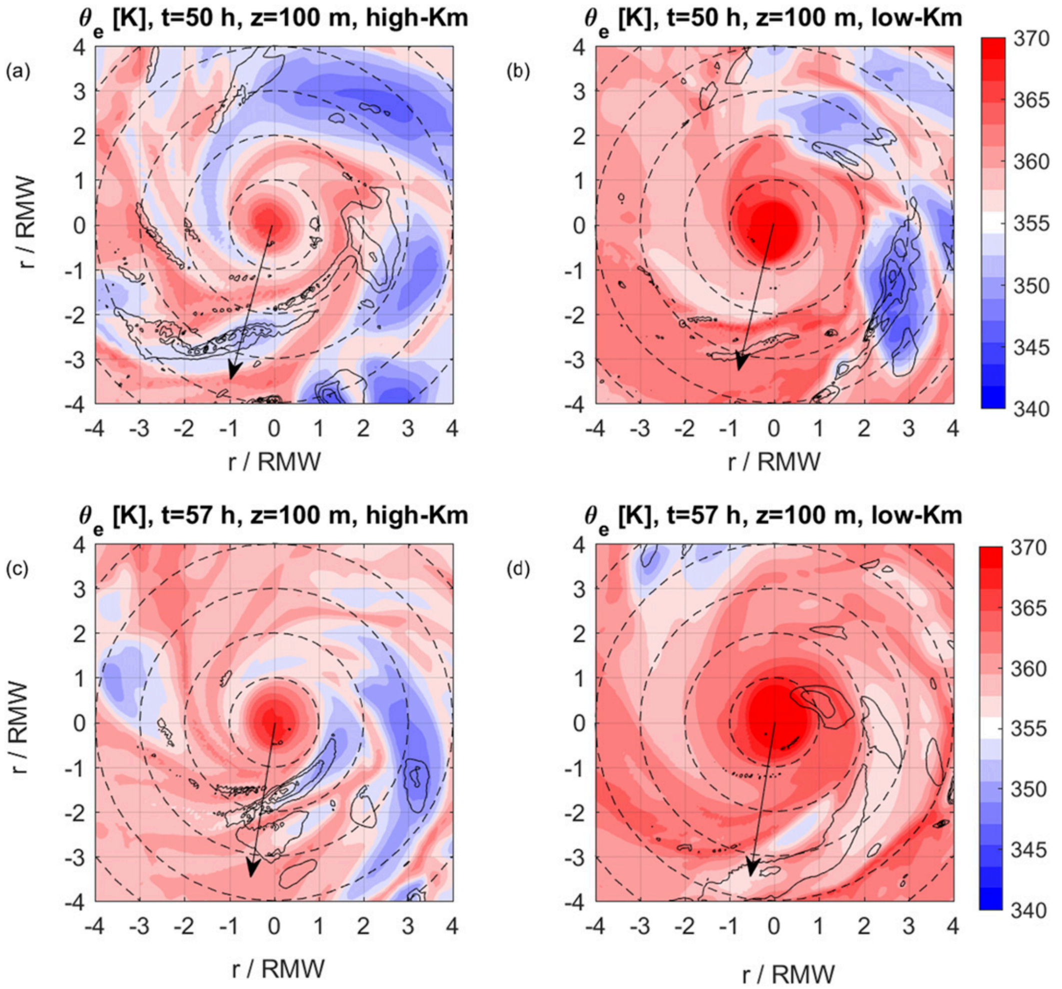

FIG. 11. Horizontal view of the equivalent potential temperature (θ_e, shading) at the height of 100 m and vertical velocity at the height of 1.5 km (contours) at (a),(b) $t = 50$ h and (c),(d) $t = 57$ h for the (left) high-K_m and (right) low-K_m forecasts. The black arrow shows the shear direction. Note that only downward motion (negative vertical velocity) is shown with a contour interval of 0.2 m s^{-1}.

recover the increase of θ_e from the upshear-left quadrant to the downshear-right quadrant for both the low-K_m and high-K_m forecasts assuming air parcel travels along the RMW (see the detailed calculation in the appendix and in Table 1). However, when air travels inward from the outer-core region ($r \sim 3r^*$) to the eyewall following an inflow trajectory, surface enthalpy fluxes are not enough to recover the increase of low θ_e from the upshear-left quadrant to the downshear-right quadrant in the high-K_m forecast, while the enthalpy fluxes are large enough for the recovery of θ_e deficit in the low-K_m forecast (see the detailed calculation in the appendix and in Table 2). This is partly because enthalpy fluxes are comparable to each other in the eyewall region, but the enthalpy fluxes are much smaller in the high-K_m forecast than in the low-K_m forecast in the outer radii (Fig. 12). At the same time, the flush of low-θ_e air from above is much less in the low-K_m forecast than in the high-K_m forecast because of a smaller tilt after the intensity divergence point (cf. Fig. 10). This is why the boundary layer entropy is much larger and more symmetrically distributed in the low-K_m forecast than in the high-K_m forecast during the second period (t = 54–59 h).

7. Discussion and conclusions

This study evaluated the role of parameterized boundary layer structure in TC intensity change in a sheared environment using HWRF retrospective forecasts. Following our previous study on the impact of K_m on the axisymmetric structure at the RI onset using

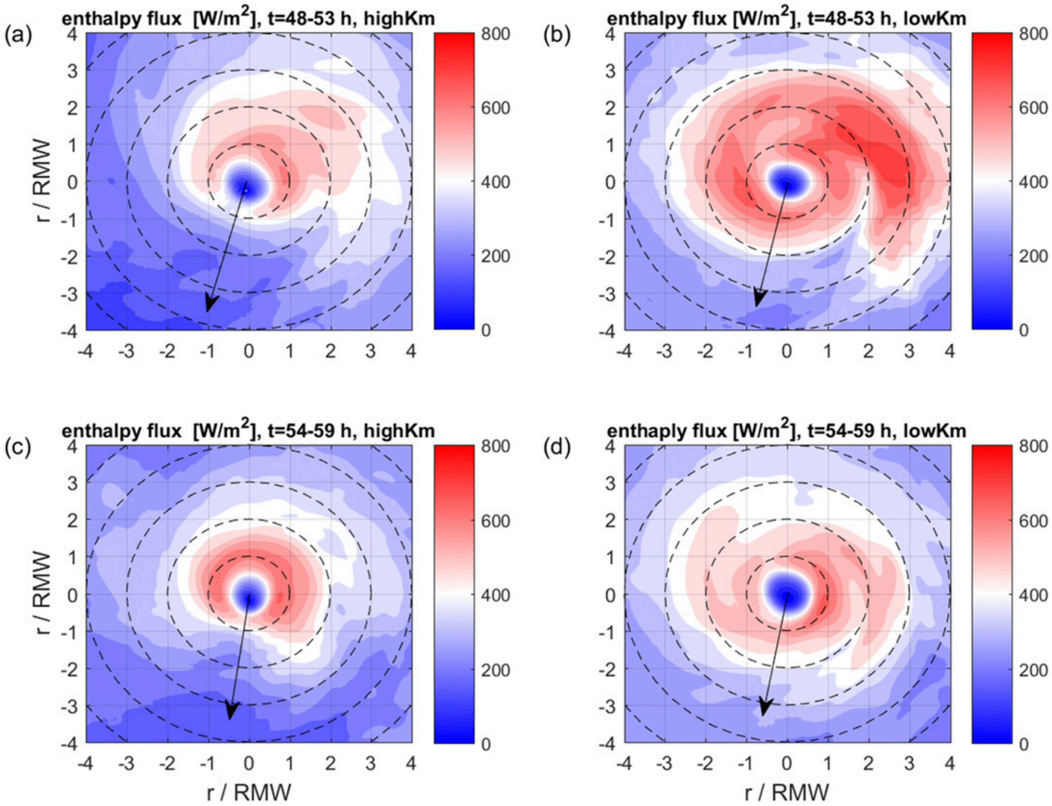

FIG. 12. Horizontal view of surface enthalpy flux (W m^{-2}) averaged during (a),(b) $t = 48$–53 h and (c),(d) $t = 54$–59 h for (left) high-K_m and (right) low-K_m forecasts of Hurricane Earl (2010). The black arrow shows the shear direction.

a composite approach, the present study used a case study approach to investigate how K_m also affects the asymmetric structure and the intensity change in two HWRF forecasts of Hurricane Earl (2010). Here, we focused on the impact of K_m on four physical processes that are related to RI: 1) angular momentum convergence, primarily by the mean flow; 2) location of convective bursts; 3) vortex tilt/precession; and 4) air–sea fluxes and PBL recovery, which is related to the tilt evolution. Our result suggests that the higher K_m leads to weaker inflow and convergence, and weaker updrafts at larger radii, resulting in a weaker vortex that is then more prone to tilting and negative thermodynamic feedbacks to the boundary layer. Here, the direct impact of K_m is the change in the boundary layer inflow and convergence; other impacts of this change can be considered as indirect impacts. The angular momentum budget analysis indicates that the convergence of angular momentum in the boundary layer that is the key dynamical process for vortex spinup is much larger in the low-K_m forecast than in the high-K_m forecast.

The case study also indicates that the parameterized boundary layer structure can modulate the convective processes in terms of the location of the convective bursts. The radial locations of the bursts are modulated by the boundary layer response to changes in K_m.

TABLE 1. A summary of the averaged values along the parcel trajectory used in Eqs. (A1)–(A4) for the boundary layer recovery of the eyewall region ($r \sim 1$RMW): F_q is the latent heat flux (W m^{-2}), F_H is the sensible heat flux (W m^{-2}), T_{LCL} is the temperature at the level of lifting condensation (K), θ_e is the equivalent potential temperature (K), θ is the potential temperature (K), $d\theta/dt$ is the calculated rate of change of θ (K h^{-1}), dq/dt is the calculated rate of change of q (g kg^{-1} h^{-1}), $d\theta_e/dt$ is the rate of change of θ_e (K h^{-1}), $\Delta\theta_e$ (ES) is the estimated change in θ_e due to surface fluxes, and $\Delta\theta_e$ (OB) is the observed change in θ_e in the model.

HWRF	θ	θ_e	T_{LCL}	F_H	F_q	$d\theta/dt$	dq/dt	$d\theta_e/dt$	$\Delta\theta_e$ (ES)	$\Delta\theta_e$ (OB)
High K_m	301.3	354.7	295.0	23.6	240.0	0.10	0.44	1.40	2.6	2.4
Low K_m	302.0	371.3	299.9	33.9	350.4	0.15	0.64	2.12	4.6	2.2

TABLE 2. A summary of the averaged values along the parcel trajectory used in Eqs. (A1)–(A4) for the boundary layer recovery of the outer-core region ($r \sim 3 \times$ RMW): F_q is the latent heat flux (W m^{-2}), F_H is the sensible heat flux (W m^{-2}), T_{LCL} is the temperature at the level of lifting condensation (K), θ_e is the equivalent potential temperature (K), θ is the potential temperature (K), $d\theta/dt$ is the calculated rate of change of θ (K h^{-1}), dq/dt is the calculated rate of change of q (g kg^{-1} h^{-1}), $d\theta_e/dt$ is the rate of change of θ_e (K h^{-1}), $\Delta\theta_e$ (ES) is the estimated change in θ_e due to surface fluxes, and $\Delta\theta_e$ (OB) is the observed change in θ_e in the model.

HWRF	θ	θ_e	T_{LCL}	F_H	F_q	$d\theta/dt$	dq/dt	$d\theta_e/dt$	$\Delta\theta_e$ (ES)	$\Delta\theta_e$ (OB)
High K_m	301.5	354.5	294.8	19.9	236.1	0.06	0.30	0.95	4.9	8.5
Low K_m	301.9	371.0	299.8	38.2	360.6	0.12	0.46	1.53	8.2	6.3

This modulation supports the idea that TCs with convective bursts located inside the low-level RMW, which preferentially occur in the low-K_m simulation, are more favorable for RI than TCs with convective bursts located primarily outside the RMW, consistent with previous observational and modeling studies. The azimuthal distribution of deep convection, which is tied to boundary layer kinematic and thermal structure, is also affected by the change in K_m in connection with vortex tilt and surface enthalpy fluxes. The more symmetric distribution of deep convection leads to larger symmetric diabatic heating inside the RMW and favors spinup of the vortex.

Our result indicates that the interaction of the TC vortex and environmental wind shear is modulated by the boundary layer structure in response to the change of K_m in the PBL scheme. The low-level and upper-level vortices tend to align after a spinup period in the low-K_m forecast, while they remain tilted most of the time and undergo precession in the high-K_m forecast. The deeper and stronger vortex that also has smaller static stability in the low-K_m forecast makes it more resilient to shear than the vortex in the high-K_m forecast. Our result suggests that PBL physics can influence the vortex tilt dynamics and its role in RI. The more symmetric deep convection may also contribute to the alignment of the vortex in the low-K_m composite following Braun et al. (2006) and Rogers et al. (2015).

Our result of the vortex tilt and the modulation of boundary layer thermodynamic structure associated with the tilt is consistent with recent theoretical studies given by Riemer et al. (2010, 2013) and Riemer (2016). In the high-K_m forecast, when the vortex tilt is large, the boundary layer θ_e is found to be much smaller than that in the low-K_m forecast. The asymmetric distribution of low-level θ_e in the shear-relative framework is also consistent with observations (Zhang et al. 2013; Zawislak et al. 2016; Nguyen et al. 2017 ; Wadler et al. 2018), in that the upshear left quadrant has the lowest θ_e that increases cyclonically to a maximum in the downshear-right quadrant, where convection is initiated in both Earl forecasts. Convective downdrafts bring down low-θ_e air from above the boundary layer in the downshear and downshear-left quadrants where the vortex tilt also occurs. As the magnitude of vortex tilt is much larger in the high-K_m forecast than in the low-K_m forecast, lower values of θ_e are flushed into the boundary layer at the outer radii. Surface enthalpy fluxes are not enough to recover the low entropy air as it spirals inward from the outer core to the eyewall region, such that the vortex weakens in the high-K_m forecast.

Above all, the differences between the two forecasts may be caused by a chain of events, such as stronger inflow bringing in more angular momentum, which accelerates the tangential winds at the top of the boundary, producing stronger updrafts at smaller radius, producing a stronger vortex which is more resistant to tilting, which also induces fewer convective downdrafts. Of note, the purpose of this study was to further understand why the recent upgrade of boundary layer physics in HWRF makes improvement in the overall intensity prediction using retrospective forecasts, notwithstanding that the PBL scheme in HWRF is far from perfect and the modification of K_m in HWRF has its own limitations (Zhang et al. 2015, 2017). Here, we emphasized the important role of boundary layer parameterization in regulating the asymmetric intensification of TCs in shear. We recommend that future model-physics upgrades in the operational HWRF and/or other forecast models should consider this important effect of model physics on TC vortex and shear interaction through multiscale physical processes, especially when the forecasts are typically performed in a cycling mode. Neglecting the consideration of multiscale interaction associated with model-physics change may introduce biases in the intensity forecasts of TCs in environmental conditions with moderate to high shear.

In a series of studies (Zhang et al. 2015, 2017; and the present study), we demonstrated why, dynamically and thermodynamically, lowering K_m in the MRF type of PBL scheme has a positive impact on HWRF forecasts of TC structure and intensity change. Lessons learned here are believed to benefit evaluation and improvement of other model physics (e.g., microphysics) in HWRF and other TC forecast models in the future.

Acknowledgment. This work was mainly supported by NOAA's Hurricane Forecast Improvement Project (HFIP) with Grants NA14NWS4680028 and NA14NWS4680030. Jun Zhang was also supported by NSF Grants AGS-1822128 and AGS-1654831, and NCAR/DTC's visitor program. We are grateful to EMC, DTC, and HRD HWRF team members for their efforts on continuously developing the HWRF Model, especially, Vijay Tallapragada, Gopal, Zhan Zhang, and Xuejin Zhang. In particular, we want to thank Young Kwon and Thiago Quirino for providing the HWRF forecasts used in this study. We want to acknowledge Leon Nguyen, Jason Sippel, and Paul Reasor for helpful suggestions to the early version of the paper. We are grateful to the editor, Ron McTaggart-Cowan for his very constructive suggestions for improving the paper. We are also grateful to Scott Braun, Roger Smith, and the other anonymous reviewer for their comments that helped improve our paper substantially.

APPENDIX

Boundary Layer Recovery Calculation

Below the description of boundary layer recovery calculation parallels those of Zhang et al. (2013). Changes in θ_e caused by surface enthalpy fluxes are obtained by applying a logarithmic differentiation to the θ_e equation:

$$\theta_e = \theta \exp\left(\frac{L_v q}{c_p T_{\mathrm{LCL}}}\right), \tag{A1}$$

and the final equation has the form of

$$\frac{d\theta_e}{dt} = \frac{\theta_e}{\theta}\frac{d\theta}{dt} + \frac{\theta_e L_v}{c_p T_{\mathrm{LCL}}}\frac{dq}{dt}, \tag{A2}$$

where θ is potential temperature; q is specific humidity; T_{LCL} is the temperature at the lifting condensation level, which can be calculated following Bolton (1980) or Davies-Jones (2009); and L_v is the latent heat of evaporation. Changes in θ and q caused by surface sensible (F_H) and latent heat (F_q) fluxes, respectively, are given by

$$\frac{d\theta}{dt} = \frac{\theta}{c_p T}\left(-\frac{1}{\rho}\frac{\partial F_{Hz}}{\partial z}\right) = \frac{\theta}{c_p T}\left(\frac{F_{H0}}{\rho \Delta z}\right), \tag{A3}$$

$$\frac{dq}{dt} = -\frac{1}{\rho L_v}\frac{\partial F_{qz}}{\partial z}\Bigr) = \frac{F_{q0}}{\rho L_v \Delta z}, \tag{A4}$$

where the subscript in the flux denotes the height (z represents the height of the measurement and 0 represents the sea surface) and Δz is the boundary layer height. Note that effects of dissipative heating, eye–eyewall mixing, and entrainment near the top of the boundary layer are not included in the above boundary layer recovery calculation.

Here, we estimate the changes in θ_e due to surface enthalpy fluxes over the period of 48–53 h in two regions: 1) the eyewall region ($r \sim 1 \times$ RMW) and 2) the outer core ($r \sim 3 \times$ RMW), and list the detailed values for Eqs. (A1)–(A4) in Tables 1 and 2, respectively. Our goal is to estimate if surface fluxes are enough to recover the θ_e deficit when air parcels move from the upshear-left quadrant to the downshear-right quadrant in the low-K_m and high-K_m forecasts during this period. Note that when moving the air parcel at the outer-core region, we consider the inflow trajectory and assumes the air parcel rises at the downshear-right quadrant in the eyewall. In the eyewall region, surface fluxes can increase θ_e by 2.6 and 4.6 K, respectively, in the high-K_m and low-K_m forecasts (Table 1), which are marginally enough to recover the observed θ_e deficit of 2.4 and 2.2 K, respectively. At the outer radii, surface fluxes can increase θ_e by 8.2 K in the low-K_m forecast (Table 2), which is enough to recover the observed θ_e deficit (6.3 K). However, surface fluxes can only increase θ_e by 4.9 K outside the eyewall region in the high-K_m forecast, which is much smaller than the observed θ_e deficit (8.5 K), suggesting that surface enthalpy fluxes are not sufficient to produce the recovery of low-θ_e air.

REFERENCES

Bolton, D., 1980: The computation of equivalent potential temperature. *Mon. Wea. Rev.*, **108**, 1046–1053, https://doi.org/10.1175/1520-0493(1980)108<1046:TCOEPT>2.0.CO;2.

Braun, S. A., 2002: A cloud-resolving simulation of Hurricane Bob (1991): Storm structure and eyewall buoyancy. *Mon. Wea. Rev.*, **130**, 1573–1592, https://doi.org/10.1175/1520-0493(2002)130<1573:ACRSOH>2.0.CO;2.

——, and W.-K. Tao, 2000: Sensitivity of high-resolution simulations of Hurricane Bob (1991) to planetary boundary layer parameterizations. *Mon. Wea. Rev.*, **128**, 3941–3961, https://doi.org/10.1175/1520-0493(2000)129<3941:SOHRSO>2.0.CO;2.

——, and L. Wu, 2007: A numerical study of Hurricane Erin (2001). Part II: Shear and the organization of eyewall vertical motion. *Mon. Wea. Rev.*, **135**, 1179–1194, https://doi.org/10.1175/MWR3336.1.

——, M. T. Montgomery, and Z. Pu, 2006: High-resolution simulation of Hurricane Bonnie (1998). Part I: The organization of eyewall vertical motion. *J. Atmos. Sci.*, **63**, 19–42, https://doi.org/10.1175/JAS3598.1.

Bryan, G. H., 2012: Effects of surface exchange coefficients and turbulence length scales on the intensity and structure of numerically simulated hurricanes. *Mon. Wea. Rev.*, **140**, 1125–1143, https://doi.org/10.1175/MWR-D-11-00231.1.

Bu, Y. P., R. G. Fovell, and K. L. Corbosiero, 2017: The influences of boundary layer vertical mixing and cloud-radiative forcing on tropical cyclone size. *J. Atmos. Sci.*, **74**, 1273–1292, https://doi.org/10.1175/JAS-D-16-0231.1.

Chen, H., and D. L. Zhang, 2013: On the rapid intensification of Hurricane Wilma (2005). Part II: Convective bursts and the upper-level warm core. *J. Atmos. Sci.*, **70**, 146–162, https://doi.org/10.1175/JAS-D-12-062.1.

——, and S. G. Gopalakrishnan, 2015: A study on the asymmetric rapid intensification of Hurricane Earl (2010) using the HWRF system. *J. Atmos. Sci.*, **72**, 531–550, https://doi.org/10.1175/JAS-D-14-0097.1.

Cione, J. J., E. A. Kalina, J. A. Zhang, and E. W. Uhlhorn, 2013: Observations of air–sea interaction and intensity change in hurricanes. *Mon. Wea. Rev.*, **141**, 2368–2382, https://doi.org/10.1175/MWR-D-12-00070.1.

Davies-Jones, R., 2009: On formulas for equivalent potential temperature. *Mon. Wea. Rev.*, **137**, 3137–3148, https://doi.org/10.1175/2009MWR2774.1.

DeMaria, M., 1996: The effect of vertical shear on tropical cyclone intensity change. *J. Atmos. Sci.*, **53**, 2076–2087, https://doi.org/10.1175/1520-0469(1996)053<2076:TEOVSO>2.0.CO;2.

Emanuel, K. A., 1995: Sensitivity of tropical cyclones to surface exchange coefficients and a revised steady-state model incorporating eye dynamics. *J. Atmos. Sci.*, **52**, 3969–3976, https://doi.org/10.1175/1520-0469(1995)052<3969:SOTCTS>2.0.CO;2.

Frank, W. M., and E. A. Ritchie, 2001: Effects of vertical wind shear on the intensity and structure of numerically simulated hurricanes. *Mon. Wea. Rev.*, **129**, 2249–2269, https://doi.org/10.1175/1520-0493(2001)129<2249:EOVWSO>2.0.CO;2.

Gall, R., J. Franklin, F. Marks, E. N. Rappaport, and F. Toepfer, 2013: The Hurricane Forecast Improvement Project. *Bull. Amer. Meteor. Soc.*, **94**, 329–343, https://doi.org/10.1175/BAMS-D-12-00071.1.

Gopalakrishnan, S. G., F. D. Marks Jr., J. A. Zhang, X. Zhang, J.-W. Bao, and V. Tallapragada, 2013: A study of the impacts of vertical diffusion on the structure and intensity of the tropical cyclones using the high-resolution HWRF system. *J. Atmos. Sci.*, **70**, 524–541, https://doi.org/10.1175/JAS-D-11-0340.1.

Guimond, S. R., G. M. Heymsfield, and F. J. Turk, 2010: Multiscale observations of Hurricane Dennis (2005): The effects of hot towers on rapid intensification. *J. Atmos. Sci.*, **67**, 633–654, https://doi.org/10.1175/2009JAS3119.1.

Hong, S., and H. Pan, 1996: Nonlocal boundary layer vertical diffusion in a medium-range forecast model. *Mon. Wea. Rev.*, **124**, 2322–2339, https://doi.org/10.1175/1520-0493(1996)124<2322:NBLVDI>2.0.CO;2.

Jiang, H., 2012: The relationship between tropical cyclone intensity change and the strength of inner-core convection. *Mon. Wea. Rev.*, **140**, 1164–1176, https://doi.org/10.1175/MWR-D-11-00134.1.

Jones, S. C., 1995: The evolution of vortices in vertical shear: Initially barotropic vortices. *Quart. J. Roy. Meteor. Soc.*, **121**, 821–851, https://doi.org/10.1002/qj.49712152406.

——, 2000: The evolution of vortices in vertical shear. III: Baroclinic vortices. *Quart. J. Roy. Meteor. Soc.*, **126**, 3161–3185, https://doi.org/10.1002/qj.49712657009.

Kaplan, J., and M. DeMaria, 2003: Large-scale characteristics of rapidly intensifying tropical cyclones in the North Atlantic basin. *Wea. Forecasting*, **18**, 1093–1108, https://doi.org/10.1175/1520-0434(2003)018<1093:LCORIT>2.0.CO;2.

——, and Coauthors, 2015: Evaluating environmental impacts on tropical cyclone rapid intensification predictability utilizing statistical models. *Wea. Forecasting*, **30**, 1374–1396, https://doi.org/10.1175/WAF-D-15-0032.1.

Kepert, J. D., 2012: Choosing a boundary layer parameterization for tropical cyclone modeling. *Mon. Wea. Rev.*, **140**, 1427–1445, https://doi.org/10.1175/MWR-D-11-00217.1.

Kilroy, G., R. K. Smith, and M. T. Montgomery, 2016: Why do model tropical cyclones grow progressively in size and decay in intensity after reaching maturity? *J. Atmos. Sci.*, **73**, 487–503, https://doi.org/10.1175/JAS-D-15-0157.1.

Leighton, H., S. Gopalakrishnan, J. A. Zhang, R. F. Rogers, Z. Zhang, and V. Tallapragada, 2018: Azimuthal distribution of deep convection, environmental factors, and tropical cyclone rapid intensification: A perspective from HWRF ensemble forecasts of Hurricane Edouard (2014). *J. Atmos. Sci.*, **75**, 275–295, https://doi.org/10.1175/JAS-D-17-0171.1.

Miyamoto, Y., and T. Takemi, 2015: A triggering mechanism for rapid intensification of tropical cyclones. *J. Atmos. Sci.*, **72**, 2666–2681, https://doi.org/10.1175/JAS-D-14-0193.1.

Molinari, J., and D. Vollaro, 2010: Rapid intensification of a sheared tropical storm. *Mon. Wea. Rev.*, **138**, 3869–3885, https://doi.org/10.1175/2010MWR3378.1.

——, J. Frank, and D. Vollaro, 2013: Convective bursts, downdraft cooling, and boundary layer recovery in a sheared tropical storm. *Mon. Wea. Rev.*, **141**, 1048–1060, https://doi.org/10.1175/MWR-D-12-00135.1.

Montgomery, M. T., and R. K. Smith, 2014: Paradigms for tropical cyclone intensification. *Aust. Meteor. Oceanogr. J.*, **64**, 37–66, https://doi.org/10.22499/2.6401.005.

——, J. A. Zhang, and R. K. Smith, 2014: An analysis of the observed low-level structure of rapidly intensifying and mature Hurricane Earl, 2010. *Quart. J. Roy. Meteor. Soc.*, **140**, 2132–2146, https://doi.org/10.1002/qj.2283.

Munsell, E. B., F. Zhang, J. A. Sippel, S. A. Braun, and Y. Weng, 2017: Dynamics and predictability of the intensification of Hurricane Edouard (2014). *J. Atmos. Sci.*, **74**, 573–595, https://doi.org/10.1175/JAS-D-16-0018.1.

Nguyen, L. T., and J. Molinari, 2012: Rapid intensification of a sheared, fast-moving hurricane over the Gulf Stream. *Mon. Wea. Rev.*, **140**, 3361–3378, https://doi.org/10.1175/MWR-D-11-00293.1.

——, ——, and D. Thomas, 2014: Evaluation of tropical cyclone center identification methods in numerical models. *Mon. Wea. Rev.*, **142**, 4326–4339, https://doi.org/10.1175/MWR-D-14-00044.1.

——, R. F. Rogers, and P. D. Reasor, 2017: Thermodynamic and kinematic influences on precipitation symmetry in sheared tropical cyclones: Bertha and Cristobal (2014). *Mon. Wea. Rev.*, **145**, 4423–4446, https://doi.org/10.1175/MWR-D-17-0073.1.

Nolan, D. S., Y. Moon, and D. P. Stern, 2007: Tropical cyclone intensification from asymmetric convection: Energetics and efficiency. *J. Atmos. Sci.*, **64**, 3377–3405, https://doi.org/10.1175/JAS3988.1.

——, J. A. Zhang, and D. P. Stern, 2009: Evaluation of planetary boundary layer parameterizations in tropical cyclones by comparison of in-situ data and high-resolution simulations of Hurricane Isabel (2003). Part I: Initialization, maximum winds, and outer core boundary layer structure. *Mon. Wea. Rev.*, **137**, 3651–3674, https://doi.org/10.1175/2009MWR2785.1.

Onderlinde, M. J., and D. S. Nolan, 2016: Tropical cyclone–relative environmental helicity and the pathways to intensification in shear. *J. Atmos. Sci.*, **73**, 869–890, https://doi.org/10.1175/JAS-D-15-0261.1.

Ooyama, K., 1969: Numerical simulation of the life cycle of tropical cyclones. *J. Atmos. Sci.*, **26**, 3–40, https://doi.org/10.1175/1520-0469(1969)026<0003:NSOTLC>2.0.CO;2.

Pendergrass, A. G., and H. E. Willoughby, 2009: Diabatically induced secondary flows in tropical cyclones. Part I: Quasi-steady forcing. *Mon. Wea. Rev.*, **137**, 805–821, https://doi.org/10.1175/2008MWR2657.1.

Reasor, P. D., and M. T. Montgomery, 2001: Three-dimensional alignment and corotation of weak, TC-like vortices via linear vortex Rossby waves. *J. Atmos. Sci.*, **58**, 2306–2330, https://doi.org/10.1175/1520-0469(2001)058<2306:TDAACO>2.0.CO;2.

——, and M. D. Eastin, 2012: Rapidly intensifying Hurricane Guillermo (1997). Part II: Resilience in shear. *Mon. Wea. Rev.*, **140**, 425–444, https://doi.org/10.1175/MWR-D-11-00080.1.

——, and M. T. Montgomery, 2015: Evaluation of a heuristic model for tropical cyclone resilience. *J. Atmos. Sci.*, **72**, 1765–1782, https://doi.org/10.1175/JAS-D-14-0318.1.

——, ——, F. D. Marks Jr., and J. F. Gamache, 2000: Low-wavenumber structure and evolution of the hurricane inner core observed by airborne dual-Doppler radar. *Mon. Wea. Rev.*, **128**, 1653–1680, https://doi.org/10.1175/1520-0493(2000)128<1653:LWSAEO>2.0.CO;2.

——, ——, and L. D. Grasso, 2004: A new look at the problem of tropical cyclones in vertical shear flow: Vortex resiliency. *J. Atmos. Sci.*, **61**, 3–22, https://doi.org/10.1175/1520-0469(2004)061<0003:ANLATP>2.0.CO;2.

——, M. D. Eastin, and J. F. Gamache, 2009: Rapidly intensifying Hurricane Guillermo (1997). Part I: Low-wavenumber structure and evolution. *Mon. Wea. Rev.*, **137**, 603–631, https://doi.org/10.1175/2008MWR2487.1.

——, R. Rogers, and S. Lorsolo, 2013: Environmental flow impacts on tropical cyclone structure diagnosed from airborne Doppler radar composites. *Mon. Wea. Rev.*, **141**, 2949–2969, https://doi.org/10.1175/MWR-D-12-00334.1.

Riemer, M., 2016: Meso-β-scale environment for the stationary band complex of vertically sheared tropical cyclones. *Quart. J. Roy. Meteor. Soc.*, **142**, 2442–2451, https://doi.org/10.1002/qj.2837.

——, and F. Laliberte, 2015: Secondary circulation of tropical cyclones in vertical wind shear: Lagrangian diagnostic and pathways of environmental interaction. *J. Atmos. Sci.*, **72**, 3517–3536, https://doi.org/10.1175/JAS-D-14-0350.1.

——, M. T. Montgomery, and M. E. Nicholls, 2010: A new paradigm for intensity modification of tropical cyclones: Thermodynamic impact of vertical wind shear on the inflow layer. *Atmos. Chem. Phys.*, **10**, 3163–3188, https://doi.org/10.5194/acp-10-3163-2010.

——, ——, and ——, 2013: Further examination of the thermodynamic modification of the inflow layer of tropical cyclones by vertical wind shear. *Atmos. Chem. Phys.*, **13**, 327–346, https://doi.org/10.5194/acp-13-327-2013.

Ritchie, E. A., and W. M. Frank, 2007: Interactions between simulated tropical cyclones and an environment with a variable Coriolis parameter. *Mon. Wea. Rev.*, **135**, 1889–1905, https://doi.org/10.1175/MWR3359.1.

Rogers, R. F., 2010: Convective-scale structure and evolution during a high-resolution simulation of tropical cyclone rapid intensification. *J. Atmos. Sci.*, **67**, 44–70, https://doi.org/10.1175/2009JAS3122.1.

——, P. Reasor, and S. Lorsolo, 2013: Airborne Doppler observations of the inner-core structural differences between intensifying and steady-state tropical cyclones. *Mon. Wea. Rev.*, **141**, 2970–2991, https://doi.org/10.1175/MWR-D-12-00357.1.

——, ——, and J. A. Zhang, 2015: Multiscale structure and evolution of Hurricane Earl (2010) during rapid intensification. *Mon. Wea. Rev.*, **143**, 536–562, https://doi.org/10.1175/MWR-D-14-00175.1.

——, J. A. Zhang, J. Zawislak, H. Jiang, G. R. Alvey, E. J. Zipser, and S. N. Stevenson, 2016: Observations of the structure and evolution of Hurricane Edouard (2014) during intensity change. Part II: Kinematic structure and the distribution of deep convection. *Mon. Wea. Rev.*, **144**, 3355–3376, https://doi.org/10.1175/MWR-D-16-0017.1.

Sanger, N. T., M. T. Montgomery, R. K. Smith, and M. M. Bell, 2014: An observational study of tropical cyclone spinup in Supertyphoon Jangmi (2008) from 24 to 27 September. *Mon. Wea. Rev.*, **142**, 3–28, https://doi.org/10.1175/MWR-D-12-00306.1.

Schecter, D. A., 2015: Response of a simulated hurricane to misalignment forcing compared to the predictions of a simple theory. *J. Atmos. Sci.*, **72**, 1235–1260, https://doi.org/10.1175/JAS-D-14-0149.1.

——, and M. T. Montgomery, 2007: Waves in a cloudy vortex. *J. Atmos. Sci.*, **64**, 314–337, https://doi.org/10.1175/JAS3849.1.

——, ——, and P. D. Reasor, 2002: A theory for the vertical alignment of a quasigeostrophic vortex. *J. Atmos. Sci.*, **59**, 150–168, https://doi.org/10.1175/1520-0469(2002)059<0150:ATFTVA>2.0.CO;2.

Schubert, W. H., and J. J. Hack, 1982: Inertial stability and tropical cyclone development. *J. Atmos. Sci.*, **39**, 1687–1697, https://doi.org/10.1175/1520-0469(1982)039<1687:ISATCD>2.0.CO;2.

——, M. T. Mongomery, R. K. Taft, T. A. Guinn, S. R. Fulton, J. P. Kossin, and J. P. Edwards, 1999: Polygonal eyewalls, asymmetric eye contraction, and potential vorticity mixing in hurricanes. *J. Atmos. Sci.*, **56**, 1197–1223, https://doi.org/10.1175/1520-0469(1999)056<1197:PEAECA>2.0.CO;2.

Shapiro, L. J., and H. E. Willoughby, 1982: The response of balanced hurricanes to local sources of heat and momentum. *J. Atmos. Sci.*, **39**, 378–394, https://doi.org/10.1175/1520-0469(1982)039<0378:TROBHT>2.0.CO;2.

Shelton, K. L., and J. Molinari, 2009: Life of a six-hour hurricane. *Mon. Wea. Rev.*, **137**, 51–67, https://doi.org/10.1175/2008MWR2472.1.

Simpson, R. H., and H. Riehl, 1958: Mid-tropospheric ventilation as a constraint on hurricane development and maintenance. *Proc. Tech. Conf. on Hurricanes,* Miami, FL, Amer. Meteor. Soc., D4.1–D4.10.

Sitkowski, M., and G. M. Barnes, 2009: Low-level thermodynamic, kinematic, and reflectivity fields of Hurricane Guillermo (1997) during rapid intensification. *Mon. Wea. Rev.*, **137**, 645–663, https://doi.org/10.1175/2008MWR2531.1.

Smith, R. K., and G. L. Thomsen, 2010: Dependence of tropical-cyclone intensification on the boundary layer representation in a numerical model. *Quart. J. Roy. Meteor. Soc.*, **136**, 1671–1685, https://doi.org/10.1002/qj.687.

——, and M. T. Montgomery, 2016: The efficiency of diabatic heating and tropical cyclone intensification. *Quart. J. Roy. Meteor. Soc.*, **142**, 2081–2086, https://doi.org/10.1002/qj.2804.

——, ——, and N. Van Sang, 2009: Tropical cyclone spin-up revisited. *Quart. J. Roy. Meteor. Soc.*, **135**, 1321–1335, https://doi.org/10.1002/qj.428.

——, J. A. Zhang, and M. T. Montgomery, 2017: The dynamics of intensification in a Hurricane Weather Research and Forecasting simulation of Hurricane Earl (2010). *Quart. J. Roy. Meteor. Soc.*, **143**, 293–308, https://doi.org/10.1002/qj.2922.

Stevenson, S. N., K. L. Corbosiero, and J. Molinari, 2014: The convective evolution and rapid intensification of Hurricane Earl (2010). *Mon. Wea. Rev.*, **142**, 4364–4380, https://doi.org/10.1175/MWR-D-14-00078.1.

Susca-Lopata, G., J. Zawislak, E. J. Zipser, and R. F. Rogers, 2015: The role of observed environmental conditions and precipitation evolution in the rapid intensification of Hurricane

Earl (2010). *Mon. Wea. Rev.*, **143**, 2207–2223, https://doi.org/10.1175/MWR-D-14-00283.1.

Tallapragada, V., C. Kieu, Y. Kwon, S. Trahan, Q. Liu, Z. Zhang, and I. Kwon, 2014: Evaluation of storm structure from the operational HWRF during 2012 implementation. *Mon. Wea. Rev.*, **142**, 4308–4325, https://doi.org/10.1175/MWR-D-13-00010.1.

Tang, B., and K. Emanuel, 2012: Sensitivity of tropical cyclone intensity to ventilation in an axisymmetric model. *J. Atmos. Sci.*, **69**, 2394–2413, https://doi.org/10.1175/JAS-D-11-0232.1.

Troen, I., and L. Mahrt, 1986: A simple model of the atmospheric boundary layer: Sensitivity to surface evaporation. *Bound.-Layer Meteor.*, **37**, 129–148, https://doi.org/10.1007/BF00122760.

Vigh, J. L., and W. H. Schubert, 2009: Rapid development of the tropical cyclone warm core. *J. Atmos. Sci.*, **66**, 3335–3350, https://doi.org/10.1175/2009JAS3092.1.

Wadler, J. B., J. A. Zhang, B. Jaimes, and L. K. Shay, 2018: Downdrafts and the evolution of boundary layer thermodynamics in Hurricane Earl (2010) before and during rapid intensification. *Mon. Wea. Rev.*, **146**, 3545–3565, https://doi.org/10.1175/MWR-D-18-0090.1.

Wang, Y., 2007: A multiply nested, movable mesh, fully compressible, nonhydrostatic tropical cyclone model—TCM4: Model description and development of asymmetries without explicit asymmetric forcing. *Meteor. Atmos. Phys.*, **97**, 93–116, https://doi.org/10.1007/s00703-006-0246-z.

Williams, G. J., Jr., 2017: The thermodynamic evolution of the hurricane boundary layer during eyewall replacement cycles. *Meteor. Atmos. Phys.*, **129**, 611–627, https://doi.org/10.1007/s00703-016-0495-4.

Zawislak, J. G., H. Jiang, G. R. Alvey, E. J. Zipser, R. F. Rogers, J. A. Zhang, and S. N. Stevenson, 2016: Observations of the structure and evolution of Hurricane Edouard (2014) during intensity change. Part I: Relationship between the thermodynamic structure and precipitation. *Mon. Wea. Rev.*, **144**, 3333–3354, https://doi.org/10.1175/MWR-D-16-0018.1.

Zhang, F., and D. Tao, 2013: Effects of vertical wind shear on the predictability of tropical cyclones. *J. Atmos. Sci.*, **70**, 975–983, https://doi.org/10.1175/JAS-D-12-0133.1.

——, and Z. Pu, 2017: Effects of vertical eddy diffusivity parameterization on the evolution of landfalling hurricanes. *J. Atmos. Sci.*, **74**, 1879–1905, https://doi.org/10.1175/JAS-D-16-0214.1.

Zhang, J. A., and W. M. Drennan, 2012: An observational study of vertical eddy diffusivity in the hurricane boundary layer. *J. Atmos. Sci.*, **69**, 3223–3236, https://doi.org/10.1175/JAS-D-11-0348.1.

——, and F. D. Marks, 2015: Effects of horizontal diffusion on tropical cyclone intensity change and structure in idealized three-dimensional numerical simulations. *Mon. Wea. Rev.*, **143**, 3981–3995, https://doi.org/10.1175/MWR-D-14-00341.1.

——, ——, M. T. Montgomery, and S. Lorsolo, 2011: An estimation of turbulent characteristics in the low-level region of intense Hurricanes Allen (1980) and Hugo (1989). *Mon. Wea. Rev.*, **139**, 1447–1462, https://doi.org/10.1175/2010MWR3435.1.

——, S. G. Gopalakrishnan, F. D. Marks, R. F. Rogers, and V. Tallapragada, 2012: A developmental framework for improving hurricane model physical parameterization using aircraft observations. *Trop. Cyclone Res. Rev.*, **1** (4), 419–429.

——, R. F. Rogers, P. D. Reasor, E. W. Uhlhorn, and F. D. Marks, 2013: Asymmetric hurricane boundary layer structure from dropsonde composites in relation to the environmental vertical wind shear. *Mon. Wea. Rev.*, **141**, 3968–3984, https://doi.org/10.1175/MWR-D-12-00335.1.

——, D. S. Nolan, R. F. Rogers, and V. Tallapragada, 2015: Evaluating the impact of improvements in the boundary layer parameterization on hurricane intensity and structure forecasts in HWRF. *Mon. Wea. Rev.*, **143**, 3136–3155, https://doi.org/10.1175/MWR-D-14-00339.1.

——, R. F. Rogers, and V. Tallapragada, 2017: Impact of parameterized boundary layer structure on tropical cyclone rapid intensification forecasts in HWRF. *Mon. Wea. Rev.*, **145**, 1413–1426, https://doi.org/10.1175/MWR-D-16-0129.1.

Zhu, P., K. Menelaou, and Z.-D. Zhu, 2014: Impact of subgrid-scale vertical turbulent mixing on eyewall asymmetric structures and mesovortices of hurricanes. *Quart. J. Roy. Meteor. Soc.*, **140**, 416–438, https://doi.org/10.1002/qj.2147.